The Impact of Stochastic Mesoscale Weather Systems on the Atlantic Ocean

SHENJIE ZHOU,[a,b] IAN A. RENFREW,[a] AND XIAOMING ZHAI[a]

[a] *Centre for Ocean and Atmospheric Sciences, School of Environmental Sciences, University of East Anglia, Norwich, United Kingdom*
[b] *British Antarctic Survey, Cambridge, United Kingdom*

(Manuscript received 20 January 2022, in final form 13 September 2022)

ABSTRACT: The ocean is forced by the atmosphere on a range of spatial and temporal scales. In numerical models the atmospheric resolution sets a limit on these scales and for typical climate models mesoscale (<500 km) atmospheric forcing is absent or misrepresented. Previous studies have demonstrated that mesoscale forcing significantly affects key ocean circulation systems such as the North Atlantic subpolar gyre (SPG) and the Atlantic meridional overturning circulation (AMOC). Here we present ocean model simulations that demonstrate that the addition of realistic mesoscale atmospheric forcing leads to coherent patterns of change: a cooler sea surface in the tropical and subtropical Atlantic Ocean and deeper mixed layers in the subpolar North Atlantic in autumn, winter, and spring. These lead to robust statistically significant increases in the volume transport of the North Atlantic SPG by 10% and the AMOC by up to 10%. Our simulations use a novel stochastic parameterization—based on a cellular automata algorithm—to represent spatially coherent weather systems realistically over a range of scales, including down to the smallest resolvable by the ocean grid (~10 km). Convection-permitting atmospheric models predict changes in the intensity and frequency of mesoscale weather systems due to climate change, so representing them in coupled climate models would bring higher fidelity to future climate projections.

KEYWORDS: North Atlantic Ocean; Atmosphere–ocean interaction; Mesoscale processes; Oceanic mixed layer; Stochastic models; Sea surface temperature

1. Introduction

The ocean is forced by the atmosphere via fluxes of heat, moisture, and momentum at the ocean's surface over a wide range of spatial and temporal scales (Sun et al. 1996; Haine et al. 2009; Holdsworth and Myers 2015; Bishop et al. 2017). In a climate model the atmospheric forcing is limited by what is represented in the atmospheric model (i.e., what is resolved or parameterized). What is resolved by the atmospheric model grid can be quantified by the "effective resolution" metric (Skamarock 2004), which makes use of the remarkable power-law characteristics of atmospheric kinetic energy (Nastrom et al. 1984; Nastrom and Gage 1985). A power spectrum of the model winds will fall away from the observed power-law relationship at its effective resolution, which is typically around $7\Delta x$, where Δx is the horizontal grid length [e.g., Fig. 11 in Skamarock (2004)]. In current global coupled climate models, the atmospheric grid resolution is typically 60 km and the oceanic grid resolution is typically $1/4°$ (Roberts et al. 2019), meaning that atmospheric features smaller than around 400 km will be absent or poorly resolved. This underrepresentation of mesoscale weather systems is a concern, as they are critical to atmosphere–ocean coupling and consequently the climate system.

Previous modeling studies have attempted to address missing mesoscale features in climate models in various ways. The obvious approach is to increase model resolution to explicitly resolve smaller-scale processes, as is exemplified in the HighResMIP (Haarsma et al. 2016) experiments of phase 6 of the Coupled Model Intercomparison Project (CMIP6); for example, in Roberts et al. (2019), their "HH" configuration has an atmospheric resolution of 25 km and an oceanic resolution of 1/12°. However, this approach is still limited by the atmospheric grid resolution and is prohibitively expensive for long simulations or large ensembles. An alternative approach is to parameterize the missing components of the atmospheric forcing in a lower-resolution framework. Previous studies have attempted to parameterize specific mesoscale weather systems, such as polar mesoscale cyclones (Condron and Renfrew 2013), orographic jets (Sproson et al. 2010), and hurricanes (Hu and Meehl 2009); while others have introduced stochastic fluctuations into the atmospheric forcing at the grid scale (Williams 2012; Li and von Storch 2013). These studies have demonstrated the importance of mesoscale atmospheric forcing for the ocean (e.g., for dense water formation in the subpolar North Atlantic; Haine et al. 2009; Sproson et al. 2010; Condron and Renfrew 2013; Jung et al. 2014; Holdsworth and Myers 2015) and as a contribution to the forcing of the AMOC (Jung et al. 2014; Roberts et al. 2019). However, there are major limitations to these previous approaches. Parameterizing specific weather systems is necessarily ad hoc and so could miss out important features, such as the impacts of tropical and midlatitude mesoscale convective systems (Schumacher and Rasmussen 2020), and

Denotes content that is immediately available upon publication as open access.

Supplemental information related to this paper is available at the Journals Online website: https://doi.org/10.1175/JCLI-D-22-0044.s1.

Corresponding author: Shenjie Zhou, shezhou@bas.ac.uk

DOI: 10.1175/JCLI-D-22-0044.1

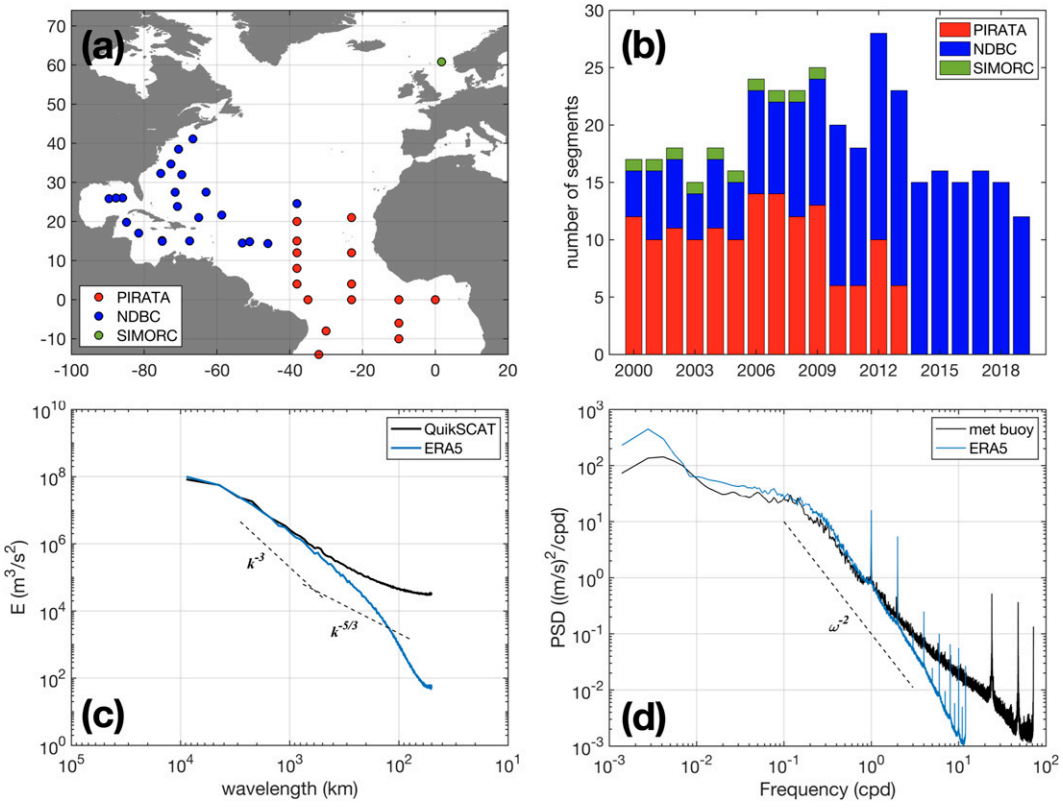

FIG. 1. Meteorological buoy availability and power spectra for the winds. (a) Locations of the meteorological buoys selected for comparison with ERA5 winds. (b) The number of meteorological buoy segments available for each year. (c) Average wavenumber spectra of QuikSCAT scatterometer and ERA5 winds. (d) Average frequency spectra of observed and ERA5 winds at grid points collocated with the meteorological buoys. The ERA5 winds fall away from the observations at the "effective resolution" of around 400–500 km and a time scale of around 12 h (2 cycles per day).

would be difficult to implement in a climate model. Adding stochastic noise at the grid scale has been a popular approach to representing the "chaotic" (i.e., unpredictable) component of the forcing field, with statistically determined constraints to match observations (Hasselmann 1976). Indeed, investigating ocean and climate responses to atmospheric variability using this approach has been explored extensively (Frankignoul and Hasselmann 1977; Barsugli and Battisti 1998; Williams 2012; Li and von Storch 2013). However, this approach does not improve the fidelity of the atmospheric forcing (i.e., the range of spatial-temporal scales is generally unimproved).

In this study, we present a novel approach to parameterize missing mesoscale atmospheric forcing that is universal, improves fidelity, and could be included within the coupling component of climate models. The rest of the paper is organized as follows. In section 2, we discuss the kinetic energy deficiency at the mesoscales in reanalysis wind fields. In section 3 we introduce a new approach to representing this mesoscale wind variability that stochastically parameterizes the "missing" kinetic energy. In section 4 we describe the ocean model configuration and the design of a small ensemble of simulations. In section 5 the improvement in atmospheric forcing and the impact on the surface fields and circulation of the Atlantic are demonstrated. Conclusions and a discussion are in section 6.

2. The mesoscale kinetic energy deficiency in reanalysis winds

An evaluation of kinetic energy is performed for wind fields obtained from the state-of-art European Centre of Mesoscale Weather Forecast (ECMWF) fifth-generation atmospheric reanalysis (ERA5; Hersbach et al. 2020). Both the wavenumber and frequency spectra are computed for ERA5 winds and compared with QuikSCAT scatterometer wind (Chelton et al. 2006) and in situ meteorological buoy wind products. In this study, we use hourly ERA5 wind fields with ~31 km horizontal resolution (Hersbach et al. 2020), mapped onto a $\frac{1}{4}^\circ \times \frac{1}{4}^\circ$ longitude–latitude grid and a daily gridded version of QuikSCAT scatterometer wind with the same $\frac{1}{4}^\circ \times \frac{1}{4}^\circ$ spatial resolution (Ricciardulli and Wentz 2015). The in situ buoy wind time series have data every 15 min and are subsampled to hourly frequency to match the ERA5 data. All the data are sampled over the North Atlantic Ocean region (100°W–20°E, 14°S–74°N) as shown in Fig. 1a.

The wavenumber spectral analyses are performed on spatially detrended wind fields from QuikSCAT scatterometer

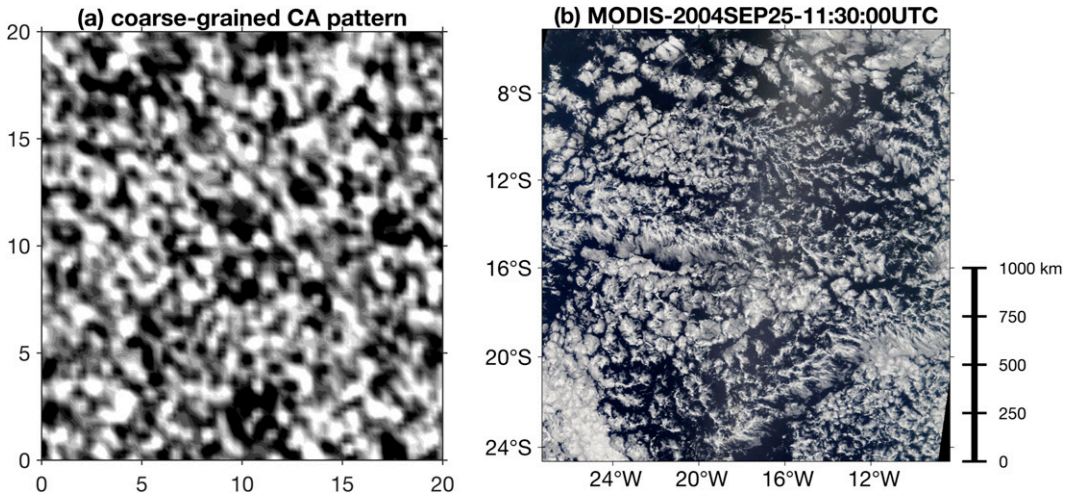

FIG. 2. Illustration of the stochastic cellular automata pattern: (a) a snapshot of the 2D perturbation pattern generated from the probabilistic CA algorithm after 3000 steps, and (b) a true-color MODIS satellite image of the tropical Atlantic Ocean that is dominated by mesoscale convective clouds on a range of scales. The CA pattern qualitatively resembles the convective cloud patterns.

observations, and ERA5 model output from January 2000 to November 2009, when QuikSCAT observations are available. Analysis is performed over the same Atlantic Ocean domain shown in Fig. 1a using a discrete Fourier transform method. A spatial detrend designed for meteorological fields over a limited area (Errico 1985) is applied on ERA5 and QuikSCAT wind fields to avoid planetary-scale features aliasing onto the mesoscale and smaller scales of the interest here. Wavenumber spectra are then computed along all suitable meridian lines to accommodate the largest possible range of wavelengths, from around 1700 km down to 25 km, the nominal grid length of the gridded daily QuikSCAT dataset. Spectra are averaged for each wavenumber bin for both ERA5 and QuikSCAT between 2000 and 2009. In total, over 1×10^8 samples are included to produce the wavenumber spectra. The frequency spectral analyses are performed on time series of buoy and ERA5 wind velocity from January 2000 to December 2019. In total 39 buoys situated within the North Atlantic domain are selected for the comparison: 16 from the Prediction and Research Moored Array in the Tropical Atlantic (PIRATA) monitoring program, 22 from the National Data Buoy Center (NDBC), and one private buoy (SIMORC) located in the Norwegian Sea (Fig. 1a). As a result, we obtain 375 year-long wind velocity time series in total from the in situ met buoy for spectral analysis (Fig. 1b). The ERA5 time series used for comparison are extracted from the nearest grid point to the buoys over years when observations are available. In total, over 3×10^6 data points are analyzed to produce the frequency spectra.

The resultant wind wavenumber spectra in Fig. 1c shows that the ERA5 surface wind kinetic energy drops away from the QuikSCAT observation, at a length scale around 400–500 km. This critical length scale coincides with the transition between the two spectral slopes, k^{-3} and $k^{-5/3}$ (where k is wavenumber), that characterize the two observed turbulence regimes (Nastrom and Gage 1985). The k^{-3} slope is associated with the large-scale coherent structures (e.g., planetary waves), while the $k^{-5/3}$ slope is thought to be associated with small-scale convection (Lilly 1983) or the generation of internal gravity waves (Dewan 1979; VanZandt 1982). The departure of the ERA5 spectra from that observed implies an underrepresentation of mesoscale variability in this reanalysis. There is also a drop off in ERA5 wind kinetic energy in the frequency domain at subdaily time scales, when compared with collocated meteorological buoy observations (Fig. 1d). Taken together these spectra suggest missing ERA5 features that exhibit spatiotemporal coherence on scales of 50–500 km and 1–24 h (Fig. 1d).

3. A new approach for parameterizing mesoscale atmospheric forcing via a cellular automata algorithm

a. *Approach*

Cellular automata (CA) algorithms use a discrete computational model to generate patterns of coherent structures over grid cells in space and time (Shutts 2005). They evolve locally through discrete states according to a set of rules applied to the states of the neighboring grid cells at the previous time step. This allows the CA algorithm to generate self-organized patterns on spatial scales that are larger than a single grid cell; in fact, coherent patterns emerge over a range of spatial scales. Originally, the rules of CA were deterministic, so the evolution of the pattern was entirely predictable. However, later adaptations led to probabilistic (or stochastic) CA where the rules incorporate a choice from a defined probability distribution. This additional stochasticity results in an "organic" looking of CA-generated perturbation pattern (Fig. 2a; Bengtsson et al. 2013) that resembles observed convective-scale weather systems (Fig. 2b). CA algorithms were first introduced to the atmospheric modeling community (Palmer 1997) to parameterize subgrid-scale disturbances. For example, in ensemble numerical weather prediction models, such stochastic CA algorithms have

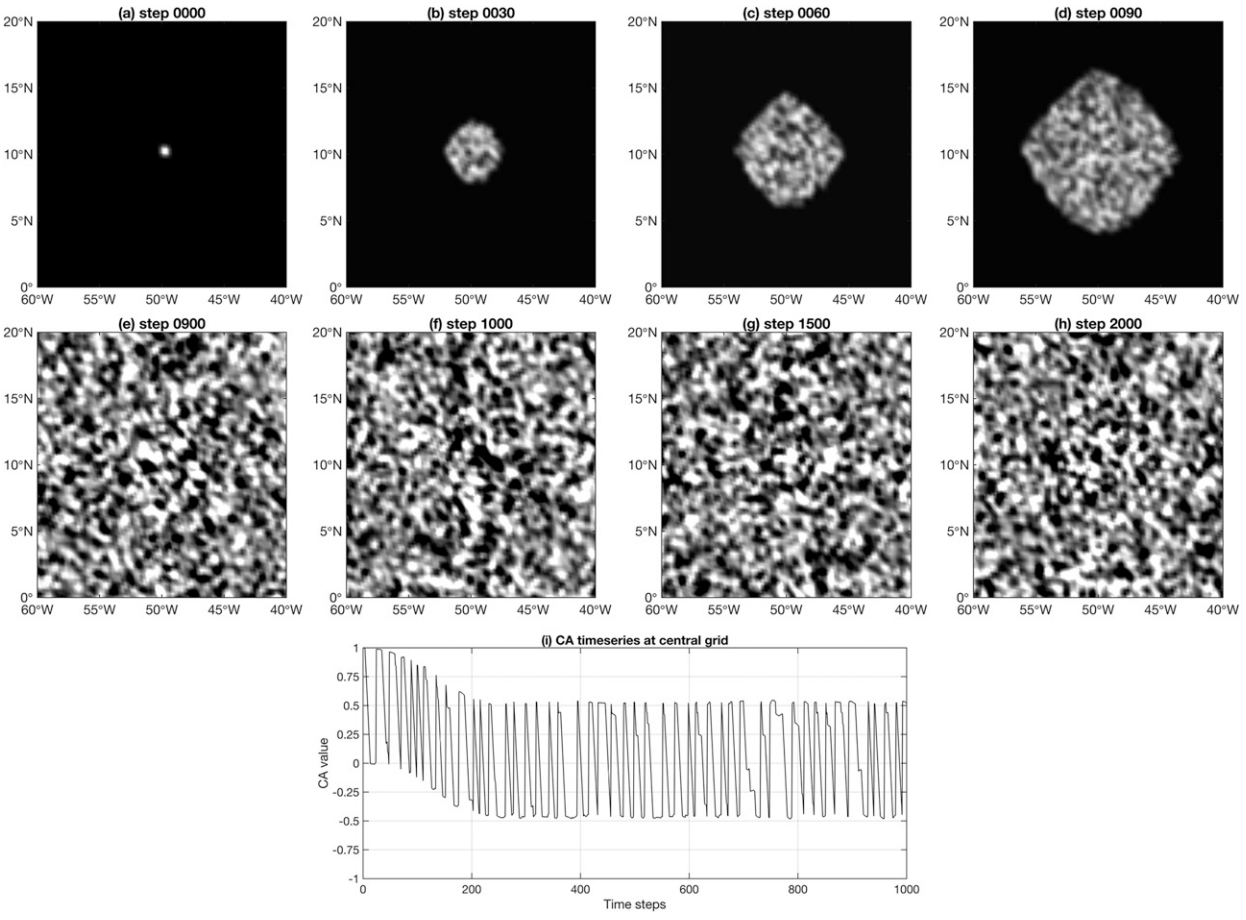

FIG. 3. Illustration of the cellular automata algorithm. (a)–(h) Snapshots of coarse-grained CA patterns from a test experiment with the NoL equal to 1. Following the spinup period in (a)–(d) the perturbation patterns resemble the snapshot of Fig. 2a and so are similar to the convective-scale cloud structures seen in satellite images (Fig. 2b). (i) This time series is the postprocessed CA perturbation for the central grid point and highlights the spinup period.

been incorporated as part of kinetic energy backscatter parameterizations to represent the effects of subgrid-scale orographic drag and gravity waves on larger-scale systems (Shutts 2005) and to simulate organized deep convection in the tropics (Bengtsson et al. 2013).

b. Implementation

The CA pattern evolves from an initial value, the "number of life" (NoL), that is assigned to certain grid cells at random locations (these cells can be regarded as "alive" while others are "dead"). The state of each grid cell at the next step is governed by rules that involve its eight neighbors, whereby the random alive cells gradually evolve into spatially coherent patterns with the surrounding cells (Fig. 3). The CA pattern is linked to the ocean model grid by two parameters: the CA grid resolution ΔS and the CA temporal increment Δt. A combination of the NoL, ΔS, and Δt parameters controls the spatial and temporal characteristics of the CA pattern that is generated, which makes it possible for a carefully calibrated CA algorithm to improve the wavenumber and frequency wind spectra at the same time as desired from the ERA5 wind fields.

For a regular 3×3, where the central cell is surrounded by eight neighboring cells, the general (deterministic) CA rules are (Shutts 2004; Bengtsson et al. 2013) as follows:

(i) For a dead grid cell surrounded by exactly 2 or 3 alive cells, at the next time step the dead cell becomes alive and is assigned with the NoL.
(ii) For an alive grid cell surrounded by exactly 3, 4, or 5 alive cells, at the next time step there are no changes.
(iii) For an alive grid cell surrounded by a different number of alive cells, at the next time step it decreases its assigned NoL by 1 until the value is equal to zero, and it is regarded as a dead grid cell.

We apply a modification to the above to incorporate probabilistic (or stochastic) CA rules. Specifically, the probabilistic rules define that for condition (i) there is only a 75% chance that the dead cells become alive, and for condition (ii) there is a 95% chance that the cell survives (i.e., the cell value remains unchanged). These probability thresholds introduce stochasticity

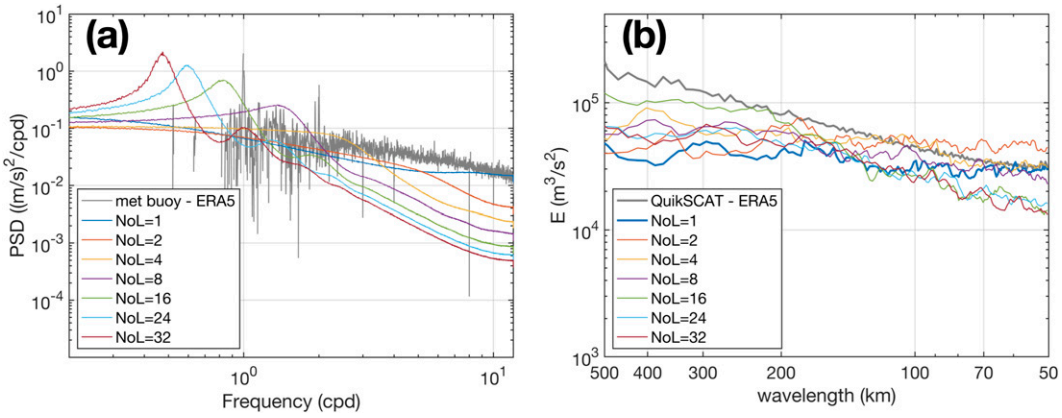

FIG. 4. Power spectra for the mesoscales. (a) The difference in frequency spectra between meteorological buoy and ERA5 winds (gray) and the same quantity computed from ERA5-CA and ERA5 winds. Unwanted frequency spectral peaks emerge in the perturbed wind field for larger values of NoL. (b) The difference in wavelength spectra between QuikSCAT and ERA5 winds (gray) and the same quantity computed from ERA5-CA and ERA5 winds with different choices of the NoL value.

and inhibit the favored new alive cell generation embedded in the original deterministic CA rule over a limited-area domain (not shown). Following Shutts (2004), the CA pattern is scaled by the NoL and coarse-grained using a 1–2–1 filter in both the zonal and meridional directions. The mean is then subtracted to make sure the spatial average of the perturbation pattern is zero.

Figures 3a and 3h show snapshots of coarse-grained CA patterns at various time steps as constrained by the probabilistic rules and with the NoL = 1. For illustrative purposes these are plotted on a latitude–longitude grid. The snapshots display the evolution of coherent spatial patterns on a variety of scales. The evolution is gradual and appears "realistic" (e.g., akin to satellite imagery of the evolution of cloud fields) (Fig. 2). Figure 3i shows a time series of postprocessed (i.e., NoL-scaled, coarse-grained, and mean-removed) CA values for a cell in the center of domain. After a spinup period over the first 200 steps, the CA evolution at the domain center levels out and the CA value flips back and forth about zero.

The addition of the CA perturbation to the wind components is via

$$u_{\mathrm{ERA5-CA}} = u_{\mathrm{ERA5}} + \mathrm{CA}(\Delta t, \Delta S, \mathrm{NoL}) \times \sigma_{\mathrm{ERA5}} \times \alpha(\mathrm{month}),$$
$$v_{\mathrm{ERA5-CA}} = v_{\mathrm{ERA5}} + \mathrm{CA}(\Delta t, \Delta S, \mathrm{NoL}) \times \sigma_{\mathrm{ERA5}} \times \alpha(\mathrm{month}). \quad (1)$$

Here the magnitude of the CA perturbation is constrained by the spatial standard deviation of ERA5 wind speed σ_{ERA5} and a nondimensional tuning parameter α. Wind direction is not preserved, but the changes in wind direction induced by the CA perturbations are relatively small due to the small magnitude of perturbation added to each wind component (see Fig. S1 in the online supplemental material). We also estimated the "best" value of α for a few subdomains (i.e., that which best fits the observed KE spectra) and found that α is not very sensitive spatially but does vary somewhat in time. Consequently, we set α to be spatially constant and to vary monthly between 0.44 and 0.49. We also considered other means of implementing the CA perturbation scheme, such as perturbing the wind streamfunction or vorticity field (e.g., Shutts 2005; Condron and Renfrew 2013), but decided to directly perturb the wind velocity field since it gives us better control of the wind KE spectra.

c. *Setting the CA parameters*

We adjust the CA grid size ΔS, CA temporal increment Δt, and the NoL to optimize the spectral characteristics of the CA perturbed winds (i.e., the ERA-CA winds). Figure 4 shows wavelength and frequency power spectra focused on the mesoscale (50–500 km) and for time scales of less than 2 days for various NoL values. Frequency spectral peaks emerge at lower frequencies with the corresponding time scale of the peaks shifting toward longer time scales as the NoL increases and are absent for small NoL such as 1 or 2 (Fig. 4a). The wavenumber spectra when the NoL is 1 also show a reasonable agreement with the difference between the QuikSCAT and ERA5 wind spectra, especially at the smallest scales down to ~50 km (Fig. 4b). Consequently, we set the NoL as 1. The choices of Δt and ΔS are determined after setting the NoL. The Δt is set pragmatically to be 1 h, the same as the ERA5 dataset. A smaller time step could be helpful for inducing higher-frequency wind variability but at a computational cost, while a larger time step would not fulfil our purpose of improving high-frequency wind variability. The ΔS is set to be 1/12°, approximately one-third of the nominal ERA5 grid (Hersbach et al. 2020), and approximately matching the ocean model grid size. This choice of ΔS introduces wind variability down to ~10-km length scales and fully utilizes the 1/10° resolution of the ocean model to capture as much small-scale variability as possible. The consequences of these parameter choices lead to a slight underrepresentation of kinetic energy around 200–500 km (Fig. 4b), which is a compromise

that we have to bear for this current version of our perturbation scheme in Eq. (1). A more scale-targeted perturbation could be developed in future work.

4. Ocean model configuration and experimental design

We use the Massachusetts Institute of Technology general circulation model (MITgcm) to investigate the Atlantic Ocean response to CA-induced wind variability. The ocean model configuration generally follows Zhai and Marshall (2013). The model has a horizontal grid size of 1/10° (i.e., eddy resolving) and a domain spanning from 14°S to 74°N and from 100°W to 20°E. There are 50 uneven vertical geopotential levels whose thickness increases from 1 m at the surface to 250 m at the bottom. The model uses a *K*-profile parameterization scheme to simulate the vertical mixing caused by surface buoyancy and momentum flux (Large et al. 1994). For simplicity, sea ice is not represented. The model was first spun up for 23 years at 1/5° resolution and then for another 30 years at 1/10° resolution, forced by climatological monthly mean forcing obtained from National Centers for Environmental Prediction–National Center for Atmospheric Research (NCEP–NCAR) reanalysis. A further spinup run is conducted for 5 years with atmospheric forcing derived from the ERA5 meteorological fields from 1995 to 1999, allowing the model to adjust to this higher-resolution forcing. The SST and sea surface salinity (SSS) are restored to monthly mean climatology, as derived from the *World Ocean Atlas 2005* (*WOA05*), on a time scale of 3 months. At the northern and southern boundaries exchanges are performed by restoring the model temperature and salinity fields toward the monthly mean *WOA05* climatological values at all depths, with a restoring time scale that varies linearly from 3 days to infinity over the 4°-wide buffer zones.

The atmospheric forcing is computed using the COARE 3.0 bulk flux algorithm (Fairall et al. 2003) using ERA5 air temperature, SST, dewpoint temperature, sea surface pressure, radiative (longwave and shortwave) heat fluxes, sea ice cover, total precipitation, and runoff. Note that the use of ERA5 meteorological variables and an offline bulk flux algorithm introduces a bias in the modeled SST when compared with climatology. This is an undesirable by-product of the ocean-only experimental design. To counter this, we apply a constant bias correction to the turbulent heat flux fields computed from a $5° \times 5°$ spatially smoothed 20-yr mean difference between the ERA5 turbulent heat fluxes and those calculated using the COARE algorithm. This bias correction is applied to all the simulations and so does not affect comparisons between them.

Four experiments are conducted—a control simulation (CONTROL) and a three-member ensemble of perturbation simulations (PERTURB1, PERTURB2, and PERTURB3)—in order to disentangle the ocean's response to CA-induced wind variability from the year 2000 onward. The CONTROL is initialized from the final output of the 5-yr spinup simulation (i.e., end of 1999) and is forced with bulk fluxes that are calculated with ERA5 winds from 1 January 2000. PERTURB1 is initialized in the same way as CONTROL but forced from 1 January 2000 with bulk fluxes computed from ERA5-CA winds. PERTURB2 is initialized with the ocean state at the end of the first-year CONTROL simulation (i.e., the end of 2000) and forced by ERA5-CA fluxes from 1 January 2001. PERTURB3 is created by cross-matching the initial ocean state and the surface forcing; it is initialized in the same way as PERTURB2 (i.e., using the ocean state from the end of the first-year CONTROL simulation) but is forced in the same way as PERTURB1 (i.e., with ERA-CA fluxes starting from 1 January 2000). Using this procedure, we effectively generate a three-member ensemble of ocean simulations. We take ensemble averages to distinguish the ocean response to the CA algorithm and that from internal variability.

5. Results

a. Atmospheric forcing changes from the CA algorithm

The CA perturbed winds demonstrate a significant improvement in spatial and temporal spectra for length scales < 400 km and time scales < 1 day (Figs. 5a,b). This spectral improvement shows that the CA perturbation induces mesoscale and high-frequency wind fluctuations at the desired length scales and time scales, thereby bringing the ERA5-CA wind field closer to observations. In addition, the CA perturbations improve the distribution of wind speed by decreasing the number of low-wind events (<7 m s^{-1}) and increasing the number of high-wind events (≥ 8 m s^{-1}; Fig. 5c) due to the nonlinear dependence of the wind speed on wind velocity components [for more details, see Zhou (2021)]. This has the effect of increasing the fraction of winds with zero bias and reducing the fraction with negative biases, at the expense of minor increases in a few of the positive bias bins (Fig. 5d). Note that the purpose of the CA perturbation is not to compensate for the wind bias in ERA5 at each individual grid point, or time, but rather to insert the right amount of additional mesoscale variability at appropriate spatial and temporal scales and with coherency, as dictated by the evolving CA pattern (Figs. 3a–h).

The CA-induced mesoscale and high-frequency wind variability enhances the surface wind speed over the entire domain (Fig. 6a). But it does so only modestly, by 0.07m s^{-1} on average, which is $<1\%$ of the mean ERA5 wind speed and $<10\%$ of the mean bias, and so within the uncertainty range of reanalyses winds. The magnitude of the wind speed increase has spatial structure, with a greater enhancement in the intertropical convergence zone (ITCZ) and subtropical gyre (STG)—regions characterized by moderate background wind speeds (<7 m s^{-1}). These regions have low wind variability in reanalyses products due to a lack of simulated mesoscale convective systems in the tropical seas (Belmonte Rivas and Stoffelen 2019) and lack of strong horizontal gradients in sea surface temperature associated with mesoscale oceanic frontal structures near the western boundary current region (Chelton et al. 2004). Overall, the CA algorithm substantially improves the fidelity of the marine wind fields: improving the power spectra, wind speed bias, and spatial distribution but without significantly changing the overall magnitude. It is worth noting that the magnitude of improvement of wind speed spatial distribution is small when compared with the actual bias between ERA5 and QuikSCAT, especially in regions

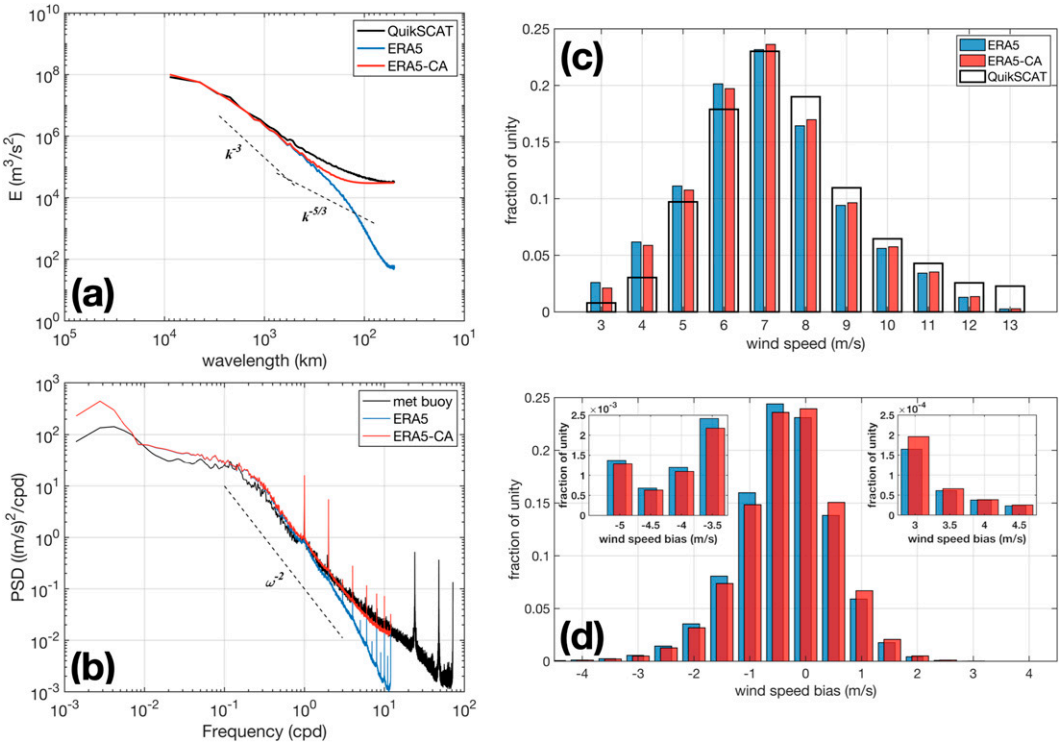

FIG. 5. Characteristics of the near-surface wind from observations, from ERA5 and from ERA5-CA, i.e., perturbed with the stochastic cellular automata algorithm. (a) Averaged wavelength spectra for near-surface wind kinetic energy derived from QuikSCAT scatterometer observations (black), ERA5 (blue), and ERA5-CA (red) from 2000 to 2009. The observed winds obey power laws for 2D turbulence theory with a k^{-3} slope over larger scales (>500 km) and a $k^{-5/3}$ over mesoscales (<400 km). (b) Frequency spectra averaged over the locations of several meteorological buoys for in situ observations, ERA5, and ERA5-CA. (c) Histogram of wind speed derived from the QuikSCAT scatterometer, ERA5, and ERA5-CA from 2000 to 2009. The CA perturbations improve the wind speed distribution by reducing the fraction of low wind speed events (<7 m s^{-1}) and increasing the fraction of high wind speed events (≥8 m s^{-1}). (d) Histogram of wind speed differences between ERA5 and QuikSCAT (blue) and between ERA5-CA and QuikSCAT (red) for the period 2000–09. The CA perturbations reduce the negative bias of the original ERA5 winds, at the expense of an increase in bias in a few of the positive bias bins.

where the ERA5 product is significantly underestimated in the ITCZ and STG (Fig. S3 in the online supplemental material), and this is mainly due to the small magnitude of CA perturbation.

The CA-induced differences in wind have a direct impact on the air–sea heat and momentum fluxes used in our ocean model experiments as these are computed offline using bulk formulas. On average, the CA perturbation systematically enhances the surface turbulent heat loss from the ocean to the atmosphere (Fig. 6b), by 1.2 W m^{-2}, due to the small average increase in wind speed. The most significant heat loss is within the region of weak background wind speeds (<7 m s^{-1}), where the greatest wind speed enhancements are located: for example, over the Gulf Stream and east tropical Atlantic where the heat loss enhancement exceeds 5 W m^{-2} (Fig. 6b). The CA perturbation also systematically enhances the wind stress across the entire North Atlantic domain (Fig. 6c). Significant increases in wind stress are found in regions of strong background wind (≥8 m s^{-1}) such as the subpolar region and midlatitude westerlies where the increase in wind stress magnitude can be more than 0.06 N m^{-2}. This is mainly because the magnitude of wind stress depends both on wind perturbations and the background wind owing to the nonlinear nature of the stress law. The strengthened wind stress over the subpolar region and midlatitude westerly region leads to anomalous anticyclonic and cyclonic wind stress curl over the STG and subpolar gyre (SPG), respectively (Fig. 6d), which reinforces the underlying wind stress curl pattern. The changes in surface heat flux and wind stress induced by the CA algorithm are comparable to those brought about by increases in model resolution—for example, differences between high-resolution and coarse-grained atmospheric forcing fields (Jung et al. 2014) and between high-resolution and low-resolution atmospheric model runs (Gavrikov et al. 2020). It is noted that the perturbation scheme presented in Eq. (1) tends to induce northeasterly or southwesterly anomalies to the original ERA5 wind field. We also tested an alternative scheme where the CA component is subtracted from the meridional wind velocity instead of being added to it. The resultant surface wind speed and more importantly wind stress (curl; see Fig. S2 in the online supplemental

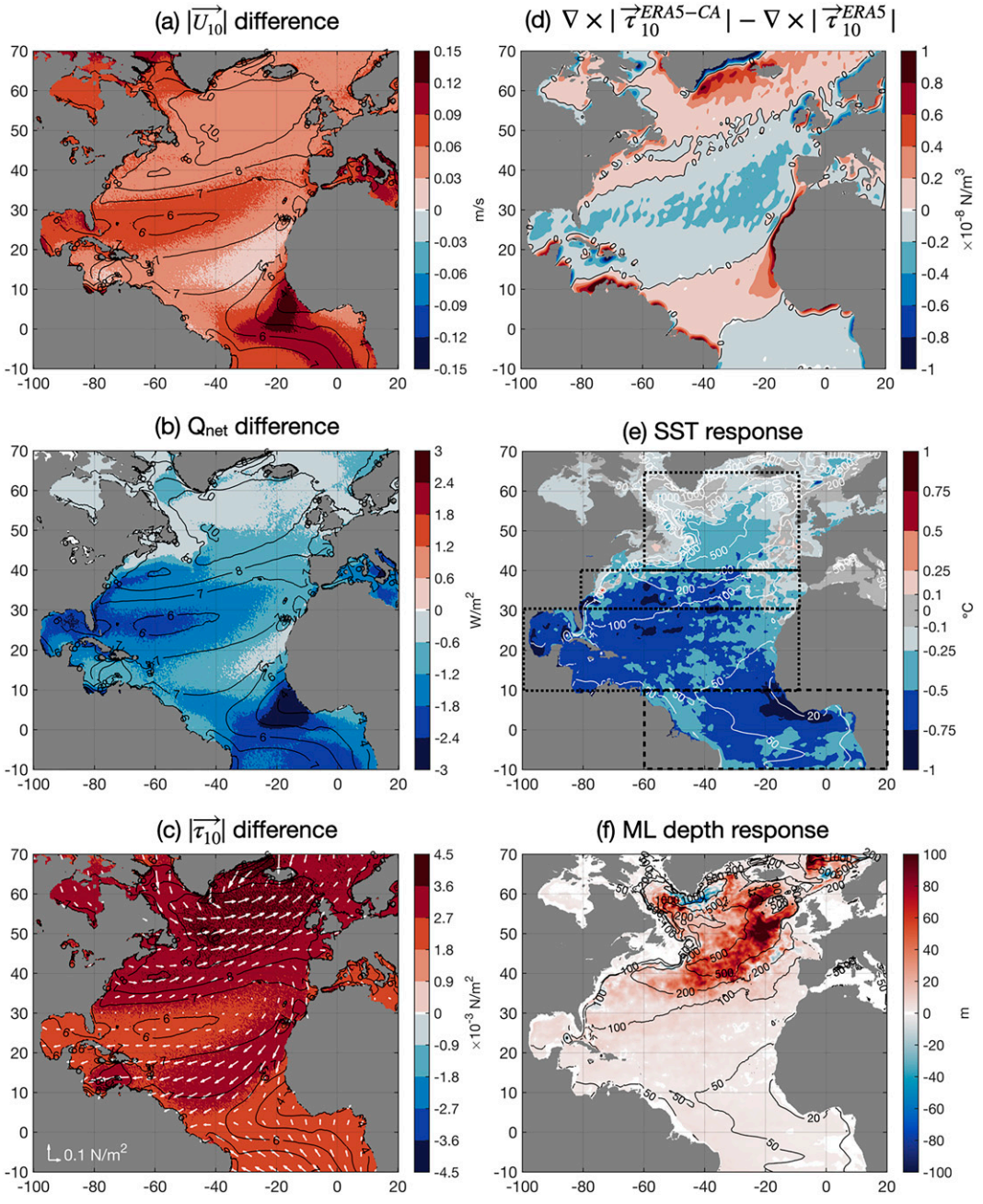

FIG. 6. CA-induced atmospheric forcing difference and surface ocean response, showing the 20-yr-mean difference in (a) wind speed, (b) net surface heat flux, (c) wind stress, and (d) wind stress curl (shading) between ERA5-CA and ERA5 (i.e., ERA5-CA minus ERA5). In (a)–(c), the black contours show the 20-yr-averaged ERA5 wind speed, and in (c) the white arrows represent the averaged wind stress vectors. Also shown is the 20-yr-mean difference in (e) SST and (f) ML depth between the PERTURB ensemble mean and CONTROL, with contours showing the ML depth in the CONTROL simulation. Dash-outlined boxes in (e) highlight four latitude bands representing the subpolar gyre, Gulf Stream, subtropical gyre, and tropical region, over which the subdomain-averaged SST response and ML depths are calculated (cf. Fig. 7, below).

material) resembles that of Fig. 6, namely, a pronounced increase of wind speed in weak wind regions and greater wind stress enhancement over strong wind regions. This implies that the distribution of the CA-induced difference in wind speed (and therefore net surface heat fluxes) and wind stress (curl) is mostly dependent on the magnitude of the background wind speed, with only secondary modulation from the relative difference between the original and perturbation wind directions. On

the other hand, Fig. S2 does show that the application of an alternative CA scheme leads to some noticeable difference in surface forcing fields in the NE trade wind region between 10° and 20°N. Future work could examine the impact of these secondary wind direction perturbation factors on the ocean but this is beyond the scope of this first study.

b. *Impact on sea surface temperature and mixed layer depth*

The response of the sea surface temperature (SST) and mixed layer (ML) depth (defined as the shallowest depth where temperature is 0.8°C colder than SST; Kara et al. 2000) to the CA-induced wind variabilities is evaluated by taking the difference of the SST and ML depth between CONTROL and ensemble mean of PERTURB1–3 to minimize the model internal variability brought by the random eddy generation.

The CONTROL simulation is sufficiently comparable to observations and a state estimate of the climatological ML depth seasonality and mean SST state particular in the tropics and subtropics (Fig. S4 in the online supplemental material). Our model overestimates ML depth in the spring, winter, and autumn, which might influence the response of the North Atlantic subpolar ocean (Fig. S4). However, in our analysis we focus on the differences between the CONTROL and perturbation simulations (PERTURB1–3), so the bias in ML depth due to ocean model configuration will be removed when the differences are examined.

The SST and ML depth differences show a systematic cooling of sea surface and a deepening of the North Atlantic's SPG ML (Figs. 6e,f). Averaged over the entire model domain, the SST drops by about 0.2°C in response to the CA-induced surface flux changes. The pronounced SST decrease is found in the ITCZ and STG, where the SST decreases by over 0.5°C when averaged mostly over the boreal summer and autumn months (Figs. 6e and 7).

The magnitude of the SST response is strongly correlated with seasonal changes in the background stratification as evidenced by the ML depth (Fig. 7). At subtropical latitudes the ML is shallow in summer and autumn, implying a small ML heat capacity, which amplifies the ML temperature response to surface buoyancy loss and/or entrainment of cold water from underneath the ML. As a result, subtropical latitudes including the interior of STG and the boundary current region as Gulf Stream region experience pronounced CA-induced SST cooling, particularly during the summer and autumn seasons. In tropical regions, the ML depth is relatively shallow all year long, which in turn leads to a large SST cooling in all four seasons (Fig. 7). Both the seasonal (Fig. S5 in the online supplemental material) and mean (Fig. 6f) difference in ML depth between the CONTROL and ensemble mean are near negligible over the tropical and subtropical region, which strongly dismisses the importance of any CA-induced ML depth changes in determining the pronounced SST response seen in these regions. The similarity between the SST response and surface heat flux differences (Figs. 6b,e) also highlights the dominant role played by surface heat flux changes in determining the SST response pattern.

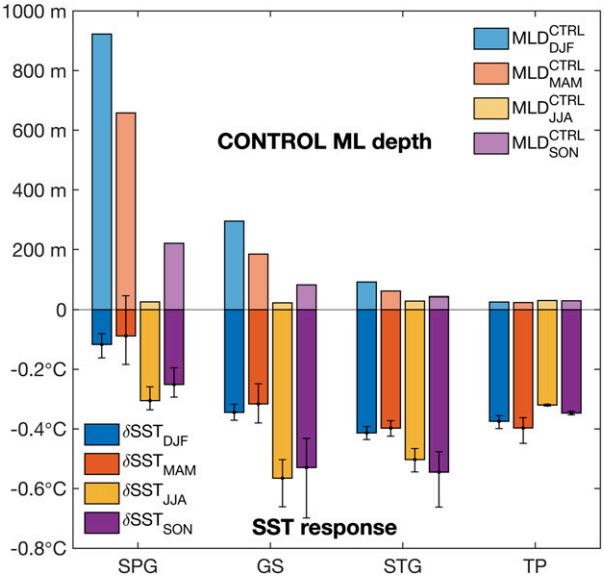

FIG. 7. Seasonally averaged ML depth and difference in SST (δSST) for the four regions of the North Atlantic. The δSST is between the three PERTURB experiments and the CONTROL. The four latitude bands are the subpolar gyre (label SPG; 40°–65°N), the Gulf Stream (GS; 30°–40°N), the subtropical gyre (STG; 10°–30°N), and the tropics (TP; 10°–10°N). The CONTROL ML depth can be regarded as an indicator of background stratification. Error bars show the upper and lower bounds of the δSST across the ensemble for each subdomain and season. Both δSST and CONTROL ML depth are averaged over four seasons distinguished by color: winter [December–February (label DJF)], spring [March–May (MAM)], summer [June–August (JJA)], and autumn [September–November (SON)].

A larger ML deepening due to the CA perturbations is commonly found north of 35°N, where the background upper ocean ML is deep (>200 m; Fig. 6f), implying that the upper ocean is weakly stratified. In the SPG region, the ML typically deepens by over 100 m (averaged annually; Fig. 6f) and by over 250 m in the winter months (supplemental Fig. S5). Because the water column in the SPG in wintertime is preconditioned with a weak vertical density gradient, the relatively small amount of additional surface buoyancy loss induced by the CA perturbations is able to trigger deep convection and this can result in a significant deepening of the ML (e.g., in the western Labrador Sea; Fig. 6e), suggesting that CA-induced mesoscale wind perturbations may have an impact on the strength and characteristics of the AMOC (Kuhlbrodt et al. 2007; Yeager et al. 2021).

c. *Impact on large-scale ocean circulation*

Current observational techniques do not facilitate an accurate estimate of the SPG based on the minimum barotropic streamfunction of the basinwide full-depth velocity field as defined in this study, so a comparison with observations was not performed directly. However, the CONTROL SPG does capture the observed interannual variability well (Fig. S6 in the online supplemental material) when comparing with an

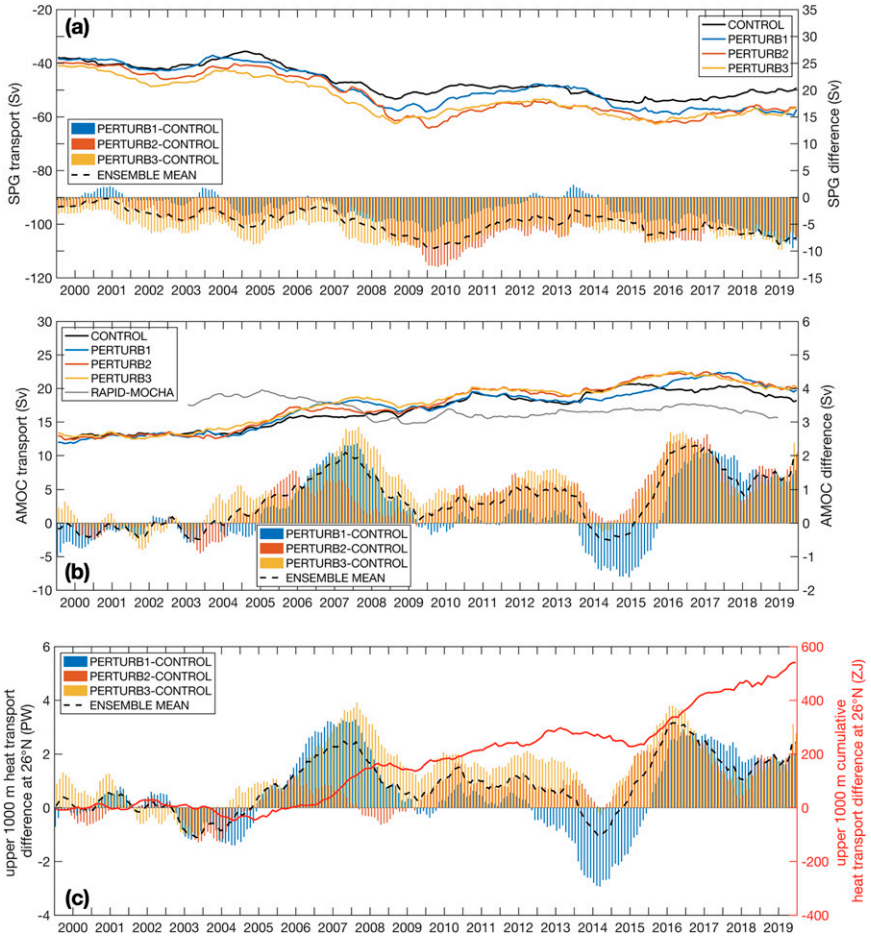

FIG. 8. CA-induced ocean circulation changes. (a) Monthly time series (thin dashed lines) of the North Atlantic SPG strength for the CONTROL (black), PERTURB1 (blue), PERTURB2 (orange), and PERTURB3 (yellow) simulations, with the corresponding 24-month running means (thick lines). The colored bars show the differences between the running means of the individual PERTURB experiments and CONTROL, and the thick dashed line shows the difference between the PERTURB ensemble mean and CONTROL (using the right-hand axis). (b) As in (a), but for the strength of the AMOC; here the RAPID AMOC observations are plotted in gray. (c) Similar to (a), but for the upper-1000-m heat transport difference at 26°N; here the red line is the cumulative heat transport (right-hand axis). The SPG and AMOC are both intensified in response to the CA perturbation, and there is enhanced poleward heat transport over the upper 1000 m as a result of the intensified AMOC.

SPG index derived from monthly sea surface height observations (Berx and Payne 2017). This suggests that the key processes dominating the SPG changes are well represented in our model configuration and justifies an assessment of the impact of the CA perturbation on the SPG strength by comparing the CONTROL and PERTURB experiments.

The intensified cyclonic wind stress curl and enhanced surface heat loss in the subpolar North Atlantic, brought about by the CA wind perturbations, lead to a strengthening of the SPG in the PERTURB simulations (Fig. 8a). The SPG strength is determined from a measure of the direct gyre rotation intensity using the minimum barotropic streamfunction within the closed contour of the monthly barotropic streamfunction field that has the largest area north of 40°N (Biri and Klein 2019). A strengthening of SPG is also found to be one of the key ocean responses to atmospheric forcing associated with mesoscale/high-frequency weather systems (Condron and Renfrew 2013; Holdsworth and Myers 2015) or forcing associated with the positive phase of the North Atlantic Oscillation (NAO+) (Eden and Willebrand 2001). All three PERTURB experiments simulate an intensified SPG circulation throughout the 20-yr period, with an ensemble-mean increase in the SPG strength of about 10% (4.6 Sv; 1 Sv = 10^6 m^3 s^{-1}). Both the two-tailed Student's t test and binomial test show that the enhancement of SPG in response to the CA-induced forcing is statistically significant with a 99% confidence level (Table 1).

The strength of AMOC presented in our study is defined as the maximum overturning streamfunction at 26°N (Danabasoglu

TABLE 1. Statistical significance (p values) for differences in the volume transport in the SPG and AMOC. Tabulated are p values of two statistical tests—a two-tailed t test and a binomial test (in parentheses)—for the difference in volume transport for the AMOC and SPG, where the difference is between the ensemble member, or the ensemble mean, and the CONTROL simulation. The tests are performed on monthly time series for the whole simulation period and for the second half of the period as well since both AMOC and SPG still experience model spinup over the first half of the period. The ensemble mean differences are statistically significant for both tests and are generally more significant for the second half of the period, while many of the PERTURB simulations are also statistically different from the CONTROL (p values less than 0.05 are in boldface font).

	Monthly (2000–19)	Monthly (2010–19)
AMOC		
PERTURB1	0.29 (0.08)	0.31 (0.31)
PERTURB2	**0.04 (<0.01)**	**<0.01 (<0.01)**
PERTURB3	**0.01 (<0.01)**	**<0.01 (<0.01)**
Ensemble mean	**0.04 (<0.01)**	**0.02 (<0.01)**
SPG		
PERTURB1	**0.04 (<0.01)**	0.07 **(<0.01)**
PERTURB2	**0.01 (<0.01)**	**<0.01 (<0.01)**
PERTURB3	**<0.01 (<0.01)**	**<0.01 (<0.01)**
Ensemble mean	**<0.01 (<0.01)**	**<0.01 (<0.01)**

et al. 2016). The AMOC simulated in the CONTROL has a strength of 17.6 ± 3.6 Sv at 26°N between 2009 and 2019, slightly higher than estimated from observations (17.0 ± 3.3 Sv) from the Rapid Climate Change–Meridional Overturning Circulation and Heatflux Array (RAPID-MOCHA; Cunningham et al. 2007) at the same latitude. Figure 8b shows that the CONTROL AMOC broadly captures the interannual variability of the RAPID-MOCHA AMOC and has a comparable standard deviation. Two [PERTURB2 (18.4 ± 2.7 Sv) and PERTURB3 (18.8 ± 2.3 Sv)] out of the three perturbation experiments simulate a consistent strengthening of the AMOC after the first 5 years, while PERTURB1 (18.0 ± 2.4 Sv) also generally simulates a strengthening of the AMOC but with a dip between 2013 and 2016 (Fig. 8b). The ensemble-mean perturbation AMOC transport is 0.4 Sv stronger than the CONTROL when averaged over the 20-yr simulation period, with transient peak increases of over 3 Sv, equivalent to over 10% of the CONTROL AMOC. Two-tailed t tests and binomial tests for the SPG and AMOC volume transport differences are statistically significant ($p < 0.01$; Table 1).

The strengthened AMOC in the PERTURB experiments leads to an increase of mean poleward heat transport of 0.8 PW (1 PW = 10^{15} W) over the top 1000 m of the modeled ocean at 26°N, 4% of the CONTROL mean heat transport of 19.6 PW, and transiently to peak increases of over 3 PW (Fig. 8c). This leads to an increase in the cumulative poleward heat transfer of over 500 ZJ (1 ZJ = 10^{21} J) from the top 1000 m after the 20-yr integration period. Part of the extra heat that is transported poleward is lost to the atmosphere and part is returned equatorward via the lower limb of the AMOC, while the remainder warms the SPG, particularly at middle depths (not shown). Enhanced northward heat transport due to a strengthened AMOC has also been reported in high-resolution coupled simulations when compared with their low-resolution counterparts (Roberts et al. 2019), suggesting that including the CA-induced wind perturbations in PERTURB brings ocean circulation changes akin to those from increased model resolution.

6. Conclusions and discussion

Our results show that adding "missing" mesoscale (10–500 km) wind variability to state-of-the-art atmospheric reanalyses used to force an ocean model can lead to systematic and significant changes in simulations of the Atlantic Ocean: its structure, large-scale circulation, and associated heat transport. The strengthened SPG and AMOC and an enhanced poleward heat transport in our CA perturbation experiments are qualitatively consistent with changes in ocean circulation found in previous studies as a result of increasing model resolution (Jung et al. 2014; Roberts et al. 2019). A key advantage of our approach is that the CA perturbation scheme is comparatively computationally inexpensive, and so has the potential to be used in long simulations or ensembles.

Our approach could be adapted to fit within the coupling component of a coupled atmosphere–ocean model. For example, a CA perturbed wind field could be generated offline and used to calculate perturbed air–sea flux fields, which are then applied as boundary conditions to both the ocean and atmospheric models. Alternatively, other stochastic physics parameterizations, such as the kinetic energy backscatter of Shutts (2005), which improves the KE spectra, could be utilized. At present, the stochastic physics in ensemble weather forecasting systems are set to taper to zero through the atmospheric boundary layer (e.g., Leutbecher et al. 2017; Walters et al. 2019). This taper could be removed over marine grid points in order to improve the representation of mesoscale winds and thus the fidelity of the atmospheric forcing of the ocean.

The intensification of the SPG and AMOC in response to the CA perturbations also resembles the ocean responses found in experiments where the ocean is forced by NAO+ related surface fluxes (Eden and Willebrand 2001; Delworth and Zeng 2016). This is because CA wind perturbations lead to strengthened westerly wind stress and enhanced surface heat loss over the SPG, features that are broadly consistent with atmospheric forcing during the NAO+ period (Marshall et al. 2001; Delworth and Zeng 2016). It is worth noting that the atmospheric forcing changes induced by the CA perturbation are a tenth of typical NAO+ forcing, while the response observed in our experiments is of the same order of magnitude as that reported from NAO+ forcing experiments (Eden and Willebrand 2001; Marshall et al. 2001; Delworth and Zeng 2016). This highlights that ocean models are highly sensitive to atmospheric forcing differences, with these sensitivities also affected by the ocean model resolution and configuration. Therefore, it calls for careful consideration of the air–sea fluxes used in high-resolution simulations of general ocean circulation, such as the AMOC (Hirschi et al. 2020).

The mesoscale "weather" components that we parameterize in this study have been recognized to be critical for both the mean state and the variability of the general ocean circulation (Condron and Renfrew 2013; Jung et al. 2014; Roberts et al. 2019) and so are key for simulating changes in ocean heat transport convergence and the resultant regional ocean heat content (Danabasoglu et al. 2016; Grist et al. 2018), for basin-scale atmosphere–ocean feedbacks (Chang et al. 1997), and for interbasin teleconnections and broader-scale climate variability (Frankignoul et al. 2017; Zhang et al. 2019). Recent convection-permitting regional atmospheric climate simulations (Kendon et al. 2014; Finney et al. 2020) predict changes in the intensity and frequency of mesoscale weather systems this century. This points to a need to represent mesoscale weather systems in coupled climate models, so that their impacts on the ocean are captured and can feed back onto the simulated changing climate system.

Acknowledgments. Our model simulations were carried out on the High-Performance Computing Cluster supported by the Research and Specialist Computing Support service at the University of East Anglia. Authors Zhou and Renfrew acknowledge partial support from the NERC Grant NE/N009754/1, a component of the Iceland Greenland Seas Project, which helped to inspire the design of this study. Zhou thanks Adrian Matthews, David Ferreira, and Xiaolong Yu for helpful discussions on this work.

Data availability statement. ERA5 atmosphere reanalysis data are available at Climate Data Store (https://cds.climate.copernicus.eu/). QuikSCAT data are produced by Remote Sensing Systems and sponsored by the NASA Ocean Vector Winds Science Team; they are available online (https://www.remss.com). NBDC and PIRATA buoy wind time series are stored at National Buoy Data Center (https://www.ndbc.noaa.gov/). SIMORC buoy data are available at System of Industry Metocean data for the Offshore and Research Communities (http://www.simorc.com/) via a data request form. The raw model output examined, code of the CA algorithm, and scripts for all analysis presented in this paper are available from author Zhou upon reasonable request.

REFERENCES

Barsugli, J. J., and D. S. Battisti, 1998: The basic effects of atmosphere–ocean thermal coupling on midlatitude variability. *J. Atmos. Sci.*, **55**, 477–493, https://doi.org/10.1175/1520-0469(1998)055<0477:TBEOAO>2.0.CO;2.

Belmonte Rivas, M., and A. Stoffelen, 2019: Characterizing ERA-Interim and ERA5 surface wind biases using ASCAT. *Ocean Sci.*, **15**, 831–852, https://doi.org/10.5194/os-15-831-2019.

Bengtsson, L., M. Steinheimer, P. Bechtold, and J.-F. Geleyn, 2013: A stochastic parametrization for deep convection using cellular automata. *Quart. J. Roy. Meteor. Soc.*, **139**, 1533–1543, https://doi.org/10.1002/qj.2108.

Berx, B., and M. R. Payne, 2017: The Sub-Polar Gyre Index—A community data set for application in fisheries and environment research. *Earth Syst. Sci. Data*, **9**, 259–266, https://doi.org/10.5194/essd-9-259-2017.

Biri, S., and B. Klein, 2019: North Atlantic sub-polar gyre climate index: A new approach. *J. Geophys. Res. Oceans*, **124**, 4222–4237, https://doi.org/10.1029/2018JC014822.

Bishop, S. P., R. J. Small, F. O. Bryan, and R. A. Tomas, 2017: Scale dependence of midlatitude air–sea interaction. *J. Climate*, **30**, 8207–8221, https://doi.org/10.1175/JCLI-D-17-0159.1.

Chang, P., L. Ji, and H. Li, 1997: A decadal climate variation in the tropical Atlantic Ocean from thermodynamic air–sea interactions. *Nature*, **385**, 516–518, https://doi.org/10.1038/385516a0.

Chelton, D. B., M. G. Schlax, M. H. Freilich, and R. F. Milliff, 2004: Satellite measurements reveal persistent small-scale features in ocean winds. *Science*, **303**, 978–983, https://doi.org/10.1126/science.1091901.

——, M. H. Freilich, J. M. Sienkiewicz, and J. M. Von Ahn, 2006: On the use of QuikSCAT scatterometer measurements of surface winds for marine weather prediction. *Mon. Wea. Rev.*, **134**, 2055–2071, https://doi.org/10.1175/MWR3179.1.

Condron, A., and I. A. Renfrew, 2013: The impact of polar mesoscale storms on northeast Atlantic Ocean circulation. *Nat. Geosci.*, **6**, 34–37, https://doi.org/10.1038/ngeo1661.

Cunningham, S. A., and Coauthors, 2007: Temporal variability of the Atlantic meridional overturning circulation at 26.5°N. *Science*, **317**, 935–938, https://doi.org/10.1126/science.1141304.

Danabasoglu, G., and Coauthors, 2016: North Atlantic simulations in Coordinated Ocean-Ice Reference Experiments Phase II (CORE-II). Part II: Inter-annual to decadal variability. *Ocean Modell.*, **97**, 65–90, https://doi.org/10.1016/j.ocemod.2015.11.007.

Delworth, T. L., and F. Zeng, 2016: The impact of the North Atlantic oscillation on climate through its influence on the Atlantic meridional overturning circulation. *J. Climate*, **29**, 941–962, https://doi.org/10.1175/JCLI-D-15-0396.1.

Dewan, E. M., 1979: Stratospheric spectra resembling turbulence. *Science*, **204**, 832–835, https://doi.org/10.1126/science.204.4395.832.

Eden, C., and J. Willebrand, 2001: Mechanism of interannual to decadal variability of the North Atlantic circulation. *J. Climate*, **14**, 2266–2280, https://doi.org/10.1175/1520-0442(2001)014<2266:MOITDV>2.0.CO;2.

Errico, R. M., 1985: Spectra computed from a limited area grid. *Mon. Wea. Rev.*, **113**, 1554–1562, https://doi.org/10.1175/1520-0493(1985)113<1554:SCFALA>2.0.CO;2.

Fairall, C. W., E. F. Bradley, J. E. Hare, A. A. Grachev, and J. B. Edson, 2003: Bulk parameterization of air–sea fluxes: Updates and verification for the COARE algorithm. *J. Climate*, **16**, 571–591, https://doi.org/10.1175/1520-0442(2003)016<0571:BPOASF>2.0.CO;2.

Finney, D. L., J. H. Marsham, D. P. Rowell, E. J. Kendon, S. O. Tucker, R. A. Stratton, and L. S. Jackson, 2020: Effects of explicit convection on future projections of mesoscale circulations, rainfall, and rainfall extremes over eastern Africa. *J. Climate*, **33**, 2701–2718, https://doi.org/10.1175/JCLI-D-19-0328.1.

Frankignoul, C., and K. Hasselmann, 1977: Stochastic climate models, Part II Application to sea-surface temperature anomalies and thermocline variability. *Tellus*, **29A**, 289–305, https://doi.org/10.3402/tellusa.v29i4.11362.

——, G. Gastineau, and Y. O. Kwon, 2017: Estimation of the SST response to anthropogenic and external forcing and its impact on the Atlantic multidecadal oscillation and the Pacific decadal oscillation. *J. Climate*, **30**, 9871–9895, https://doi.org/10.1175/JCLI-D-17-0009.1.

Gavrikov, A., and Coauthors, 2020: RAS-NAAD: 40-yr high-resolution North Atlantic atmospheric hindcast for multipurpose

applications (new dataset for the regional mesoscale studies in the atmosphere and the ocean). *J. Appl. Meteor. Climatol.*, **59**, 793–817, https://doi.org/10.1175/JAMC-D-19-0190.1.

Grist, J. P., S. A. Josey, A. L. New, M. Roberts, T. Koenigk, and D. Iovino, 2018: Increasing Atlantic Ocean heat transport in the latest generation coupled ocean–atmosphere models: The role of air–sea interaction. *J. Geophys. Res. Oceans*, **123**, 8624–8637, https://doi.org/10.1029/2018JC014387.

Haarsma, R. J., and Coauthors, 2016: High Resolution Model Intercomparison Project (HighResMIP v1.0) for CMIP6. *Geosci. Model Dev.*, **9**, 4185–4208, https://doi.org/10.5194/gmd-9-4185-2016.

Haine, T. W. N., S. Zhang, G. W. K. Moore, and I. A. Renfrew, 2009: On the impact of high-resolution, high-frequency meteorological forcing on Denmark Strait ocean circulation. *Quart. J. Roy. Meteor. Soc.*, **135**, 2067–2085, https://doi.org/10.1002/qj.505.

Hasselmann, K., 1976: Stochastic climate models Part I. Theory. *Tellus*, **28A**, 473–485, https://doi.org/10.3402/tellusa.v28i6.11316.

Hersbach, H., and Coauthors, 2020: The ERA5 global reanalysis. *Quart. J. Roy. Meteor. Soc.*, **146**, 1999–2049, https://doi.org/10.1002/qj.3803.

Hirschi, J. J.-M., and Coauthors, 2020: The Atlantic meridional overturning circulation in high resolution models. *J. Geophys. Res. Oceans*, **125**, e2019JC015522, https://doi.org/10.1029/2019JC015522.

Holdsworth, A. M., and P. G. Myers, 2015: The influence of high-frequency atmospheric forcing on the circulation and deep convection of the Labrador Sea. *J. Climate*, **28**, 4980–4996, https://doi.org/10.1175/JCLI-D-14-00564.1.

Hu, A., and G. A. Meehl, 2009: Effect of the Atlantic hurricanes on the oceanic meridional overturning circulation and heat transport. *Geophys. Res. Lett.*, **36**, L03702, https://doi.org/10.1029/2008GL036680.

Jung, T., S. Serrar, and Q. Wang, 2014: The oceanic response to mesoscale atmospheric forcing. *Geophys. Res. Lett.*, **41**, 1255–1260, https://doi.org/10.1002/2013GL059040.

Kara, A. B., P. A. Rochford, and H. E. Hurlburt, 2000: An optimal definition for ocean mixed layer depth. *J. Geophys. Res.*, **105**, 16 803–16 821, https://doi.org/10.1029/2000JC900072.

Kendon, E. J., N. M. Roberts, H. J. Fowler, M. J. Roberts, S. C. Chan, and C. A. Senior, 2014: Heavier summer downpours with climate change revealed by weather forecast resolution model. *Nat. Climate Change*, **4**, 570–576, https://doi.org/10.1038/nclimate2258.

Kuhlbrodt, T., A. Griesel, M. Montoya, A. Levermann, M. Hofmann, and S. Rahmstorf, 2007: On the driving processes of the Atlantic meridional overturning circulation. *Rev. Geophys.*, **45**, RG2001, https://doi.org/10.1029/2004RG000166.

Large, W. G., J. C. McWilliams, and S. C. Doney, 1994: Oceanic vertical mixing: A review and a model with nonlocal boundary layer parameterization. *Rev. Geophys.*, **32**, 363–403, https://doi.org/10.1029/94RG01872.

Leutbecher, M., and Coauthors, 2017: Stochastic representation of model uncertainties at ECMWF: State of the art and future version. *Quart. J. Roy. Meteor. Soc.*, **143**, 2315–2339, https://doi.org/10.1002/qj.3094.

Li, H., and J.-S. von Storch, 2013: On the fluctuating buoyancy fluxes simulated in a 1/10° OGCM. *J. Phys. Oceanogr.*, **43**, 1270–1287, https://doi.org/10.1175/JPO-D-12-080.1.

Lilly, D. K., 1983: Stratified turbulence and the mesoscale variability of the atmosphere. *J. Atmos. Sci.*, **40**, 749–761, https://doi.org/10.1175/1520-0469(1983)040<0749:STATMV>2.0.CO;2.

Marshall, J., H. Johnson, and J. Goodman, 2001: A study of the interaction of the North Atlantic oscillation with ocean circulation. *J. Climate*, **14**, 1399–1421, https://doi.org/10.1175/1520-0442(2001)014<1399:ASOTIO>2.0.CO;2.

Nastrom, G. D., and K. S. Gage, 1985: A climatology of atmospheric wavenumber spectra of wind and temperature observed by commercial aircraft. *J. Atmos. Sci.*, **42**, 950–960, https://doi.org/10.1175/1520-0469(1985)042<0950:ACOAWS>2.0.CO;2.

——, ——, and W. H. Jasperson, 1984: Kinetic energy spectrum of large-and mesoscale atmospheric processes. *Nature*, **310**, 36–38, https://doi.org/10.1038/310036a0.

Palmer, T. N., 1997: On parametrizing scales that are only somewhat smaller than the smallest resolved scales, with application to convection and orography. *Proc. ECMWF Workshop on New Insights and Approaches to Convective Parametrization*, Reading, United Kingdom, ECMWF, 328–337, https://www.ecmwf.int/node/11493.

Ricciardulli, L., and F. J. Wentz, 2015: A scatterometer geophysical model function for climate-quality winds: QuikSCAT Ku-2011. *J. Atmos. Oceanic Technol.*, **32**, 1829–1846, https://doi.org/10.1175/JTECH-D-15-0008.1.

Roberts, M. J., and Coauthors, 2019: Description of the resolution hierarchy of the global coupled HadGEM3-GC3. 1 Model as used in CMIP6 HighResMIP experiments. *Geosci. Model Dev.*, **12**, 4999–5028, https://doi.org/10.5194/gmd-12-4999-2019.

Schumacher, R. S., and K. L. Rasmussen, 2020: The formation, character and changing nature of mesoscale convective systems. *Nat. Rev. Earth Environ.*, **1**, 300–314, https://doi.org/10.1038/s43017-020-0057-7.

Shutts, G. J., 2004: A stochastic kinetic energy backscatter algorithm for use in ensemble prediction systems. ECMWF Tech. Memo. 449, European Centre for Medium-Range Weather Forecasts, 26 pp., https://doi.org/10.21957/74ucsdm5c.

——, 2005: A kinetic energy backscatter algorithm for use in ensemble prediction systems. *Quart. J. Roy. Meteor. Soc.*, **131**, 3079–3102, https://doi.org/10.1256/qj.04.106.

Skamarock, W. C., 2004: Evaluating mesoscale NWP models using kinetic energy spectra. *Mon. Wea. Rev.*, **132**, 3019–3032, https://doi.org/10.1175/MWR2830.1.

Sproson, D. A. J., I. A. Renfrew, and K. J. Heywood, 2010: A parameterization of Greenland's tip jets suitable for ocean or coupled climate models. *J. Geophys. Res.*, **115**, C08022, https://doi.org/10.1029/2009JC006002.

Sun, J., J. F. Howell, S. K. Esbensen, L. Mahrt, C. M. Greb, R. Grossman, and M. A. LeMone, 1996: Scale dependence of air–sea fluxes over the western equatorial Pacific. *J. Atmos. Sci.*, **53**, 2997–3012, https://doi.org/10.1175/1520-0469(1996)053<2997:SDOASF>2.0.CO;2.

VanZandt, T. E., 1982: A universal spectrum of buoyancy waves in the atmosphere. *Geophys. Res. Lett.*, **9**, 575–578, https://doi.org/10.1029/GL009i005p00575.

Walters, D., and Coauthors, 2019: The Met Office Unified Model Global Atmosphere 7.0/7.1 and JULES Global Land 7.0 configurations. *Geosci. Model Dev.*, **12**, 1909–1963, https://doi.org/10.5194/gmd-12-1909-2019.

Williams, P. D., 2012: Climatic impacts of stochastic fluctuations in air–sea fluxes. *Geophys. Res. Lett.*, **39**, L10705, https://doi.org/10.1029/2012GL051813.

Yeager, S., and Coauthors, 2021: An outsized role for the Labrador Sea in the multidecadal variability of the Atlantic overturning circulation. *Sci. Adv.*, **7**, eabh3592, https://doi.org/10.1126/sciadv.abh3592.

Zhai, X., and D. P. Marshall, 2013: Vertical eddy energy fluxes in the North Atlantic subtropical and subpolar gyres. *J. Phys. Oceanogr.*, **43**, 95–103, https://doi.org/10.1175/JPO-D-12-021.1.

Zhang, R., R. Sutton, G. Danabasoglu, Y. O. Kwon, R. Marsh, S. G. Yeager, D. E. Amrhein, and C. M. Little, 2019: A review of the role of the Atlantic meridional overturning circulation in Atlantic multidecadal variability and associated climate impacts. *Rev. Geophys.*, **57**, 316–375, https://doi.org/10.1029/2019RG000644.

Zhou, S., 2021: The ocean's response to stochastic atmospheric forcing. Ph.D. thesis, University of East Anglia, 146 pp., https://ueaeprints.uea.ac.uk/id/eprint/81487.